Probing Shear-Banding Transitions of the VCM Model for Entangled Wormlike Micellar Solutions Using Large Amplitude Oscillatory Shearing (LAOS) Deformations

Lin Zhou,[a] L.Pamela Cook,[b] Gareth H. McKinley[c]

[a] *Department of Mathematics, New York City College of Technology, Brooklyn, NY,* 11201

[b] *Department of Mathematical Sciences, University of Delaware, Newark, DE.* 19716

[c] *Department of Mechanical Engineering, Massachusetts Institute of Technology, Cambridge, MA.* 02139

Abstract

We explore the use of Large Amplitude Oscillatory Shear (LAOS) deformation to probe the dynamics of shear-banding in soft entangled materials, primarily wormlike micellar solutions which are prone to breakage and disentanglement under strong deformations. The state of stress in these complex fluids is described by a class of viscoelastic constitutive models which capture the key linear and nonlinear rheological features of wormlike micellar solutions, including the breakage and reforming of an entangled network. At a frequency-dependent critical strain, the imposed deformation field localizes to form a shear band, with a phase response that depends on the frequency and amplitude of the forcing. The different material responses are com-

pactly represented in the form of Lissajous (phase plane) orbits and a corresponding strain-rate and frequency-dependent Pipkin diagram. Comparisons between the full network model predictions and those of a simpler, limiting case are presented.

Key words: LAOS, Pipkin diagram, shear banding

1 Introduction

It is well-known that many classes of complex fluids including micellar solutions, entangled melts and densely-packed colloidal suspensions develop spatial inhomogeneities or 'shear bands' when undergoing strong shearing deformations [1, 2]. Recently there have been numerous experimental investigations that have documented the details of these banding transitions in simple steady shearing flow [3, 4, 5, 6]. Kinematic measurements in a rheometric device such as a cone-plate rheometer or cylindrical Couette device show that the homogeneous viscometric flow observed at low deformation rates spontaneously develops a banded profile beyond a critical deformation rate, typically with a region of high shear rate located close to the (inner) moving surface and a region of much lower shear rate near the stationary surface. As the shear rate increases, the extent of the high shear rate band broadens until it encompasses the entire gap [5, 7, 8]. Careful experimental observations in entangled micellar solutions [9] as well as recent calculations [10] show that the dynamical response of these bands can be very complex with the shear-banded fluid region exhibiting traveling internal waves or even chaotic fluctuations in the

Email addresses: lzhou@citytech.cuny.edu (Lin Zhou,), cook@math.udel.edu (L.Pamela Cook,), gareth@mit.edu (Gareth H. McKinley).

measured stress. Simultaneous measurements of the macroscopic 'flow curve' (steady shear stress versus imposed shear rate) typically show a stress plateau in this regime. This banding can be thought of generically as a phase-transition between two different microscopic configurations that can coexist at the same stress [11, 12, 13]. A number of excellent reviews on shear banding in wormlike micelles and other complex fluids have recently been presented [1, 2, 14].

This steady state banding behavior can be emulated by a number of different rheological equations of state (EoS) which incorporate non-local effects arising from the coupling between the macroscopic stress and the local conformation of the microstructural elements [12, 13, 15, 16, 17]. A key feature of the majority of these constitutive models (but not [17]) is the presence of a nonmonotonic relationship between the imposed deformation rate and the resulting macroscopic stress, *if* the flow is assumed *a priori* to be homogeneous. In the shear-banded region this homogeneous solution is unstable under appropriate boundary conditions on the velocity, and the local velocity field across the sample gap bifurcates into two separate kinematic 'phases'.

Although non-monotonicity in the constitutive relation between stress and shear rate is important for describing the onset of shear-banding in the local kinematics and the appearance of a plateau in the measured macroscopic 'flow curve', it is an insufficient criterion for differentiating between the responses of different constitutive models. Some candidate EoS, the Johnson-Segalman model for example, exhibit nonphysical responses in rapidly-varying deformations [18]; other models do not exhibit proper linear viscoelastic behavior in the limit of small deformations. The VCM class of models [16] do predict appropriate behavior in shear, step strain and also in extensional flows [19][20]. In this paper we examine the response of the VCM constitutive model in Large

Amplitude Oscillatory Shear (LAOS) [21] and compare with a limiting case of the model, the PEC model. Very recently, Adams and Olmsted [17] have considered LAOS flows for the 'Rolie-Poly' model of monodisperse entangled polymeric melts and solutions. They show that transient inhomogeneous responses similar to steady state shear-banding can develop in simulations under large imposed deformations.

We consider LAOS deformations in a cylindrical Couette cell with an imposed (inner cylinder) displacement of the form $d/h = \gamma_0 \sin(\omega t)$, where h is the rheometer gap width. The principal utility of LAOS is that the deformation amplitude γ_0 and time scale ω^{-1} can be varied independently. For small amplitude oscillations (SAOS) the shear stress response is a phase-shifted sinusoid $\sigma = \sigma_0 \sin(\omega t + \delta)$ in which the amplitude and phase of the response depend on the frequency. However in LAOS, when nonlinearities are important, the temporal response is more complex; consisting of multiple harmonic components with both the phase and the amplitude depending nonlinearly on the driving frequency and the imposed strain. If the system shear-bands then these coefficients will also vary with the spatial position. Fourier series expansions of the response have been used to decompose the elastic and viscous responses [21, 22]. A recent framework proposed by Ewoldt *et al.* [23] uses instead a more natural Chebyshev decomposition. The material response at the moving cylindrical wall is decomposed as $\sigma'(t;\omega,\gamma_0) = \gamma_0 \Sigma_k (e_k(\omega,\gamma_0) T_k(sin(\omega t)) + \omega \nu_k(\omega,\gamma_0) T_k(cos(\omega t)))$ where T_k are the Chebyshev polynomials of order k (and only the odd coefficients in this expansion are nonzero [23]). The number of non-zero coefficients $e_k, \eta_k = \omega \nu_k$, and their relative magnitudes, may provide a fingerprint of the nonlinear viscoelastic material response.

In this paper we examine the LAOS response of a prototypical class of models (the VCM model) for shear-banding fluids in order to better understand how these models describe the shear-banding events observed experimentally under oscillatory forcing and to understand how the banded structures described by these models evolve progressively in a well-controlled unsteady shearing deformation as the strain amplitude and driving frequency increase.

2 The Model Formulation

To explore the dynamics of shear-banding in LAOS we consider a family of constitutive models developed to describe wormlike micellar solutions. These models are self-consistently derived from kinetic network theory and accurately capture the coupling between the local microstructural conformation and the resulting macroscopic stress response [16, 19]. This family of models, referred to as VCM for brevity, captures individual contributions to the total viscoelastic stress arising from long entangled chains (species 'A') and from a shorter, unentangled 'B' species. The local number densities n_A, n_B respectively of the longer and shorter chains evolve due to dynamic breaking and reforming events.

The dimensionless governing equations for the VCM model are [19]:
for the number densities;

$$\mu\frac{Dn_A}{Dt} = 2\delta_A\nabla^2 n_A - \delta_A\nabla\nabla : \mathbf{A} + \frac{c_B}{2}n_B^2 - c_A n_A \tag{1a}$$

$$\mu\frac{Dn_B}{Dt} = 2\delta_B\nabla^2 n_B - 2\delta_B\ \nabla\nabla : \mathbf{B} - c_B n_B^2 + 2c_A n_A \tag{1b}$$

and for the stress contributions;

$$\mu \mathbf{A}_{(1)} + \mathbf{A} - n_A \mathbf{I} - \delta_A \nabla^2 \mathbf{A} = c_B n_B \mathbf{B} - c_A \mathbf{A} \tag{2a}$$

$$\epsilon\mu \mathbf{B}_{(1)} + \mathbf{B} - \frac{1}{2} n_B \mathbf{I} - \epsilon\delta_B \nabla^2 \mathbf{B} = \epsilon(-2\, c_B n_B \mathbf{B} + 2\, c_A \mathbf{A}) \tag{2b}$$

where $(\cdot)_{(1)}$ indicates the upper convected derivative defined as

$$(\cdot)_{(1)} = \frac{\partial(\cdot)}{\partial t} + \mathbf{v} \cdot \nabla(\cdot) - ((\nabla \mathbf{v})^t \cdot (\cdot) + (\cdot) \cdot \nabla \mathbf{v}). \tag{3}$$

Here the reforming rate c_B is assumed to be a constant ($c_B = c_{Beq}$), and the breakage rate $c_A = c_{Aeq} + \frac{\xi}{3}(\dot{\boldsymbol{\gamma}} : \frac{\mathbf{A}}{n_A})$ where c_{Aeq} is a constant. In this system, time has been nondimensionalized by the effective relaxation time $\lambda_{eff} = \frac{\lambda_A}{1+c'_{Aeq}\lambda_A}$ where λ_A is the reptative time of species A. It is clear from this expression that the relaxation time of the entangled micellar network is reduced from the reptation time due to breakage, which represents another relaxation mechanism of the system. The other characteristic scales for the system are as follows: the velocity is scaled by λ_{eff}/h where h is the gap width, the stresses are scaled by the plateau modulus and the number densities are scaled by the equilibrium number density of species A. The model parameters are the non-dimensional diffusion constants $\delta_A = D_A\lambda_A/h^2$ and $\delta_B = D_B\lambda_A/h^2$, the Deborah number De which measures the relaxation time of the fluid to the time of the motion of the fluid (and which with this scaling appears in the boundary conditions), the ratio of the relaxation time of species B to that of species A, $\epsilon = \lambda_B/\lambda_A$, the ratio of the relaxation time of species A in the absence of scission and reforming (reptation time) to the effective relaxation time of the solution when scission and reforming dynamics are included, $\mu = \lambda_A/\lambda_{eff}$. Additional parameters are the scaled equilibrium breaking and reforming rates, c_{Aeq}, c_{Beq} and the single nonlinear parameter ξ controlling the dynamic breakage rate. The effect of varying the magnitude of these parameter values on the model predictions is explored in [16].

With this nondimensionalization the total micellar stress is,

$$\boldsymbol{\sigma} = \mathbf{A} + \mathbf{2B}. \tag{4}$$

and the total stress is given by

$$\boldsymbol{\Pi} = p\mathbf{I} + (n_A + n_B)\mathbf{I} - \mathbf{A} - 2\mathbf{B} - \beta\dot{\boldsymbol{\gamma}} \tag{5}$$

in which $\dot{\boldsymbol{\gamma}} = \nabla\mathbf{v} + (\nabla\mathbf{v})^t$. Here $\beta = \eta_s/(\eta_s + \eta_p)$ where η_p is the contribution of the entangled micelles to the total zero shear rate viscosity of the micellar mixture and η_s is the solvent viscosity. For almost all micellar preparations this parameter is small (order of 10^{-5}) since the solvent is water or another low viscosity fluid. These constitutive equations for the state of stress must be coupled to the equations of conservation of mass:

$$\nabla \cdot \mathbf{v} = \mathbf{0} \tag{6}$$

and that of (inertialess) conservation of momentum:

$$\nabla \cdot \boldsymbol{\Pi} = \mathbf{0}. \tag{7}$$

We guarantee conservation of mass in our geometry by the assumption of a unidirectional shearing flow $v_\theta(r, t)$.

If equilibrium breaking and reforming events are disallowed ($c_{Aeq} = c_{Beq} = 0$), and there is only the 'A' species in the model ($n_A \equiv 1$ and $n_B \equiv 0$), then the model still describes shear-banding transitions (when momentum is included), plus a corresponding plateau in the steady shear flow-curve, as a result of non-affine deformation of the elastic network and disentanglement of the longer 'A' chains. In this *non-breaking limit* the model involves fewer material constants and evolution equations. If additionally the short chains comprising the 'B' species have vanishingly small relaxation time, $\lambda_B \to 0$, then their rheological

response is essentially Newtonian; in this limit the constitutive equation reduces to a nonlocal generalization of the partially-extending convected (PEC) equation proposed by Larson [24] as a differential analog of the Doi-Edwards reptation model for entangled melts. For this limit the evolution equation for the extra stress that arises from the entangled microstructure plus the momentum equation are,

$$\mathbf{A}_{(1)} + \mathbf{A} + \delta\nabla\mathbf{A} - \mathbf{I} = -\frac{1}{3}\xi(\dot{\boldsymbol{\gamma}} : \mathbf{A})\mathbf{A} \tag{8}$$

$$\nabla \cdot (P\mathbf{I} - \beta_{PEC}\dot{\boldsymbol{\gamma}} - (\mathbf{A} - \mathbf{I})) = 0. \tag{9}$$

For this limiting (single species) model, the total shear stress is written $\sigma_{r\theta} = -A_{r\theta} - \beta_{PEC}\dot{\gamma}$, where the ratio of the viscosity contribution from the inelastic 'B' species (η_B) to the total zero-shear-rate viscosity of the system is denoted $\beta_{PEC} = \eta_B/(\eta_A + \eta_B)$. The value of β_{PEC} controls the extent of the shear-banding domain (which is controlled by the number density of (short) B species in the VCM model) and varies with the type of entangled fluid being considered. For example Tapadia & Wang [7] consider LAOS deformation for an entangled solution of high molecular weight polybutadiene in a viscous low molecular weight (and unentangled) oligomeric oil. In such a system the long chains cannot break (in contrast to an entangled wormlike micellar system) although they can still disentangled leading to formation of transient shear bands with complex dynamics [6, 17].

In the present study we seek to compare and contrast the LAOS response of the PEC and VCM models in order to understand which features of these transient shear banding dynamics are common to the two systems and which are connected to rupture events in the entangled network. We use the following values in our PEC computations; $\beta_{PEC} = 5 \times 10^{-3}$, $\xi = 0.7$. The parameters

we use for the VCM model calculation are shown in the caption to Fig.1. The value of ξ is chosen to be the same as that of the PEC model, and the parameters μ and ϵ are adjusted to match the value of the plateaus predicted by the two models. The geometric curvature parameter $p = \frac{h}{R_i}$ (where h is the gap width and R_i is the inner cylinder radius) is taken as $p = 0.1$ for both the PEC and the VCM model calculations. Fig. 1 shows the steady state flow curves for the VCM and the PEC model in Taylor-Couette flow with our parameter choices. In this computation we have added a small amount of diffusion ($\delta_A = \delta_B = 0.001$ for the VCM model and $\delta = 0.001$ for the PEC model) in order to obtain a unique plateau [19]. For these parameters the steady state shear stresses and shear stress plateau agree well and the flow curves are in good agreement for applied shear rates $De = \lambda_A \dot{\gamma} \leq 10^2$.

The VCM model equations (and the corresponding PEC model equations) are solved numerically using a spectral method with Chebyshev polynomials as the base functions. Convergent results are obtained for $N \geq 20$. Increasing N yields more accurate local solutions; we pick $N = 201$, so that the banding region is well resolved. The spatiotemporal dynamics of the shear-banding transition arise through the coupling of the momentum equation with the constitutive equation [19]. In these transient computations, the history dependence of the solution is incorporated, thus the numerical solutions are uniquely determined without the necessity of incorporating diffusive terms, which serve primarily to smooth the interface between the two different 'kinematic phases'. Addition of diffusive terms results in a transition region of size $\delta_A^{1/2}$ [16, 19].

The oscillatory deformation history is applied at the inner rigid cylinder, and the outer cylinder is held stationary. With the present scalings, the material

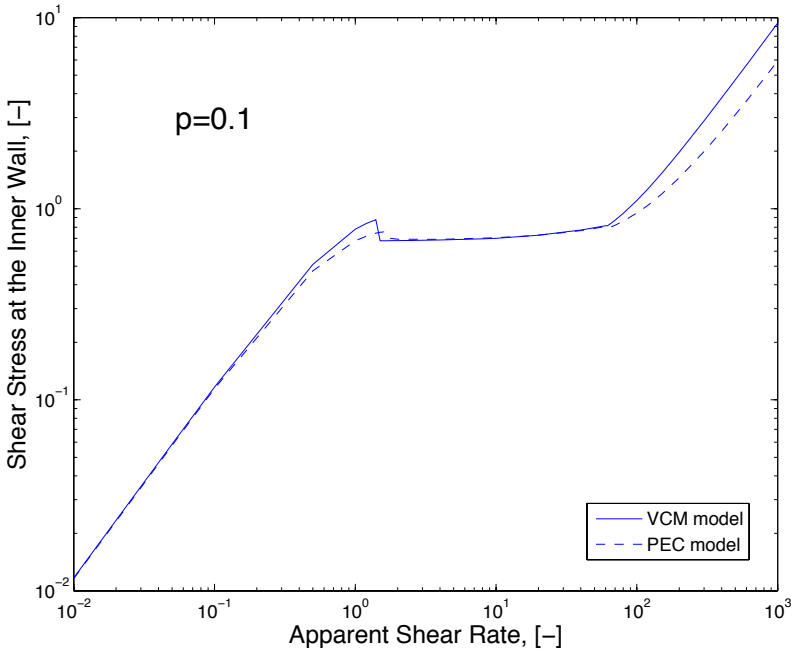

Fig. 1. Steady state flow curves for the VCM (solid curve) and the PEC (dashed curve) models in cylindrical Couette flow. Parameter choices for each model are as follows: the PEC model, $\xi = 0.7$, $\beta_{PEC} = 0.005$; the VCM model, $\xi = 0.7$, $\beta = 6.78 \times 10^{-5}$, $\epsilon = 4.5 \times 10^{-4}$, $n_B^0 = \exp(1/8)$, $\mu = 5.7$, $c_{Aeq} = \mu - 1 = 4.7$, $c_{Beq} = 2c_{Aeq}/(n_B^0)^2 = 7.3$.

response is a function of the dimensionless frequency or *Deborah number* $De = \lambda_A \omega$ and the imposed strain amplitude γ_0. The dimensionless (apparent) shear rate or *Weissenberg number* $Wi \equiv De\gamma_0 = \lambda_A \omega \gamma_0$ is also useful in representing the material response.

3 Results and Discussion

The fully-developed material response to the sinusoidal deformation history is shown for the VCM model for several representative frequency and shear rate

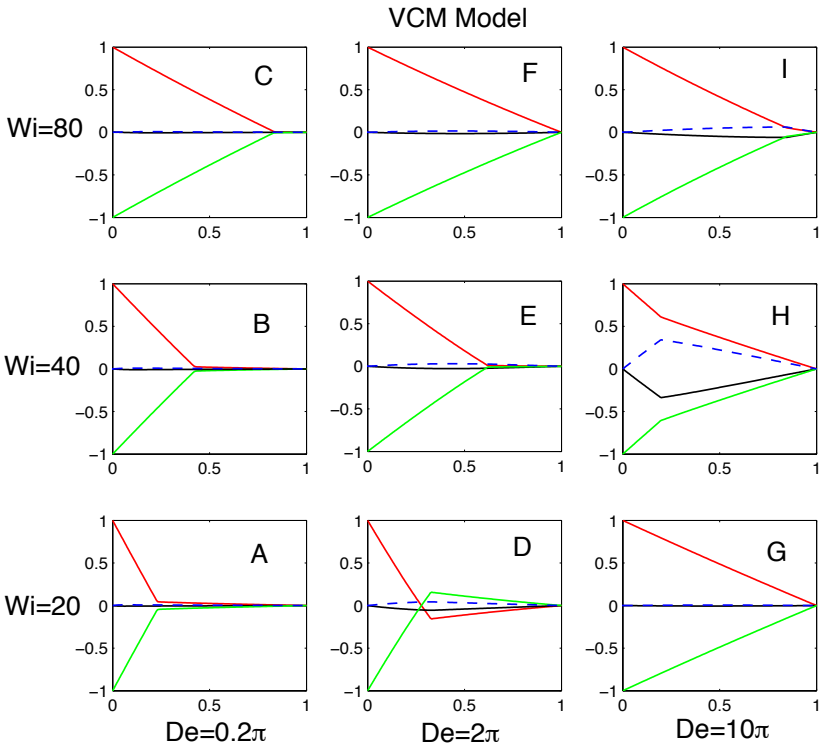

Fig. 2. Normalized VCM (v/v_w) velocity profiles across the normalized gap $0 \leq y \leq 1$ of the circular Couette cell showing shear banding, the progressive growth of the shear-band across the gap, and the phase response of the fluid velocity for various values of De, Wi. The profiles shown are at the instant when the wall velocity ($v/v_w = \cos\omega t$) is maximum (red), minimum (green), zero and increasing (dashed, blue), and zero and decreasing (solid,black), after all initial transients have decayed. Responses shown are at frequencies $De = 0.2\pi, 2\pi, 10\pi$ each for strain rates of $Wi = 20, 40, 80$. The model parameters for the VCM model are given in Fig. 1. The letter inscribed in each plot locates the response on the Pipkin diagram (Fig. 7).

pairs (De, Wi) in Fig.2. The velocity profiles shown are the fully-developed periodic responses at the maximum/minimum wall speeds $t = 0, \frac{\pi}{De}, \frac{2\pi}{De}$... and at the maximum wall deflections $t = \frac{\pi}{2De}, \frac{3\pi}{2De}$....

For small apparent strains (e.g. Fig.2:G $\gamma_0 = Wi/De = 20/(10\pi) \approx 0.6$) the

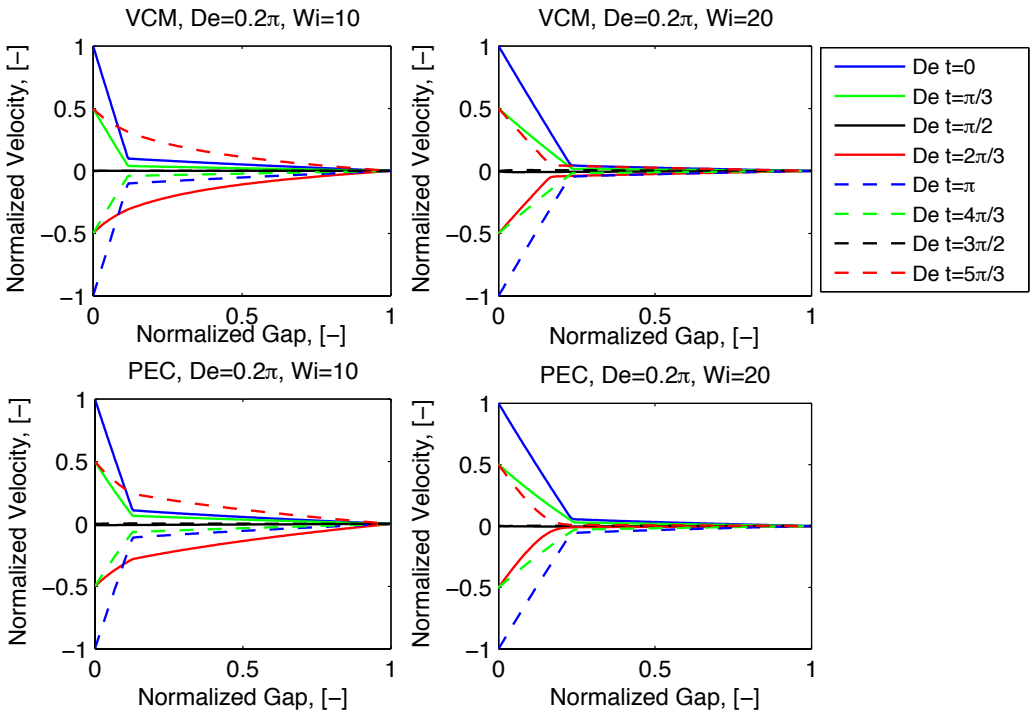

Fig. 3. Velocity profile snapshots for the VCM (upper row) and PEC (lower row) model simulations at selected times in the cycle as shown. These responses are at low frequencies ($De = 0.2\pi$)and shear rates of $Wi = 10, 20$ within the shear banding region.

'linear' viscoelastic limit is recovered, and the velocity field in the fluid varies linearly (to within curvature effects $p = \frac{h}{R_i}$) across the gap, in phase with the boundary velocity, so that $v(y,t)/v_w \approx (1-y)\cos(De\ \mathrm{t}) + O(p)$, where $y = (r - r_i)/h$ and $v_w = Wi$ is the maximum velocity at the inner wall of the rheometer.

The material response is more interesting under stronger forcing (larger strain). For a fixed frequency De, the velocity response develops shear bands as the dimensionless strain rate Wi increases, with a high shear rate band forming near the inner cylinder and the fraction of the gap containing the high shear rate band increasing proportionally with Wi (e.g. Fig.2: A, B, C) until even-

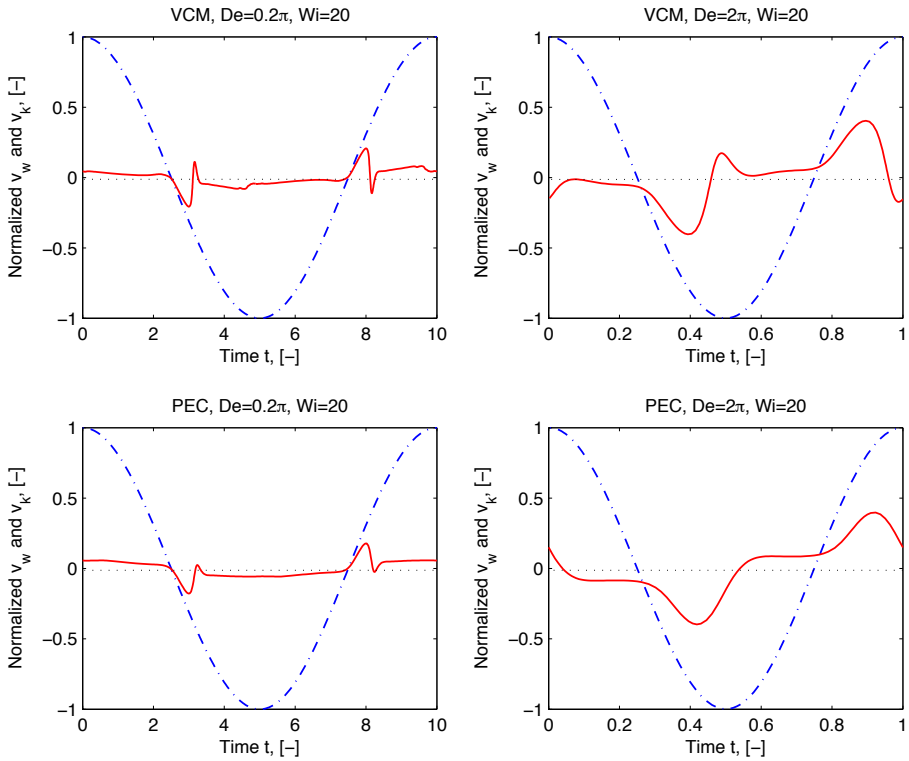

Fig. 4. The scaled (imposed) LAOS wall velocity, $\cos(De\,t)$ (dash dot line) and the scaled velocity of the kink between the two shear bands (solid line) are shown as functions of time over a cycle in the fully developed response. The results are shown at a slow ($De = 0.2\pi$) and a faster ($De = 2\pi$) forcing frequency at a shear rate of $Wi = 20$.

tually the high shear rate band spans the entire gap (e.g. for $De = 0.2\pi$, this happens at $Wi = 94$, which is not shown). For a fixed shear rate Wi, as the oscillatory frequency De increases, the profiles vary nonmonotonically and elastic recoil events become more and more prominent. The elastic recoil is evidenced in Fig. 2: D and H. Similar recoil events have been described in experimental measurements of transient shear banding [25].

The dynamics of these shear banding regions are shown more clearly in Figs. 3,

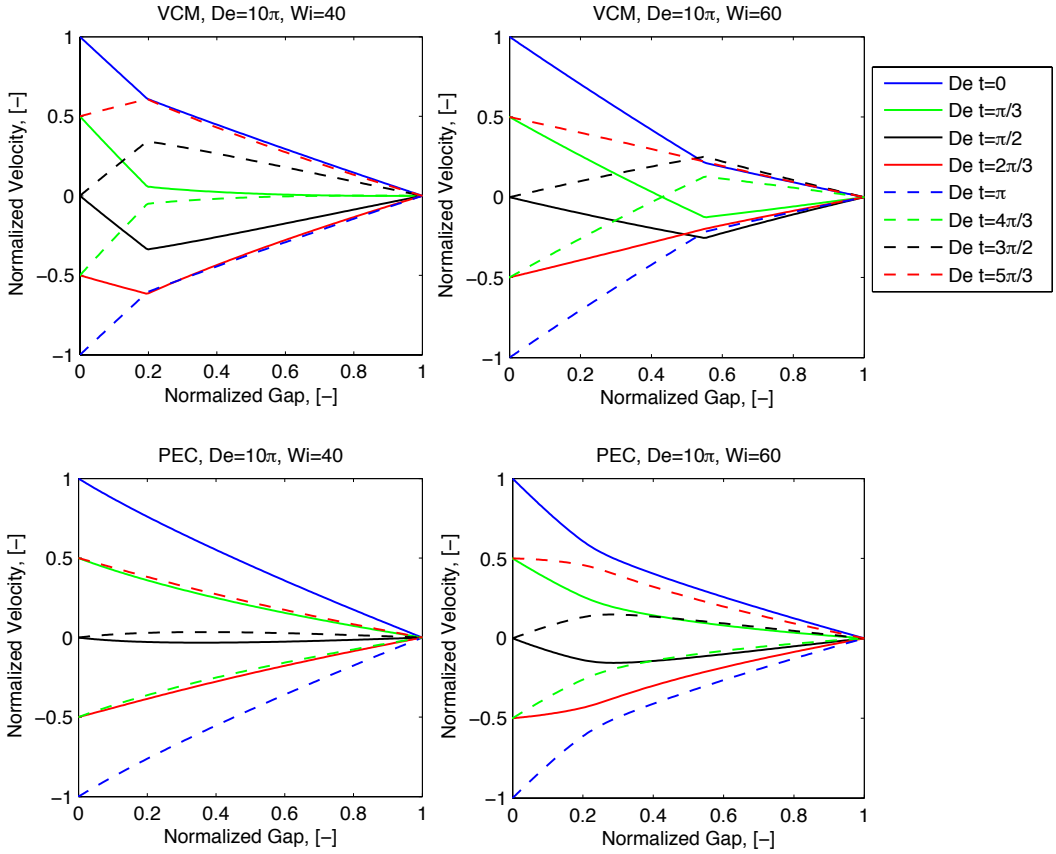

Fig. 5. Snapshots of the velocity profile for the VCM (upper row) and PEC (lower row) model simulations at selected times in the cycle as shown. These responses are at high frequencies ($De = 10\pi$) and shear rates of $Wi = 40, 60$ (corresponding to strains of $4/\pi, 6/\pi$) within the shear banding region of the VCM model.

4, 5 where the spatial and temporal evolution of the velocity profiles are shown at several frequencies and shear rates for both the VCM and PEC models. In Figs. 3, 5 velocities are shown at eight selected times throughout a cycle. In Fig. 3 the frequency is selected to be slow enough that the response is quasi-steady ($De = 0.2\pi$) and the shear rates are $Wi = 10, 20$. As noted previously, the constitutive parameters of the two models are chosen so that the steady state flow curves agree closely (see Fig. 1), and we see that at low frequencies

the dynamics of the shear banding are similar for both models except in mid cycle, $De\,t = 2\pi/3, 5\pi/3$ (red) at the higher shear rate, $Wi = 20$. At this specific time within the shearing cycle the velocity profile of the VCM model is more sharply kinked at the location of the shear band, whereas the velocity profile in the PEC model is not as sharp. This is a consequence of the higher value of β_{PEC} and the larger viscous (diffusive) stresses in the PEC model.

In Fig. 4 the cyclic variation of the imposed wall velocity and the instantaneous velocity of the kink between the shear bands are shown over one cycle for the VCM and PEC models for both a slow ($De = 0.2\pi$) and a faster ($De = 2\pi$) oscillatory deformation at a shear rate of $Wi = 20$. Because the Weissenberg number is the same in each case, our expectations based on steady shearing (Fig. 1) would be that the response of two models should be identical. At the slower forcing frequency the kink velocity is small and in phase with the imposed wall motion with the exception of a small excursion and then recoil near $t = 2\pi/(3De)$, $5\pi/(3De)$. When the wall stops moving and changes direction, during this short period of relaxation there is a stored elastic stress in the fluid which leads to a brief local flow reversal of the shear band. A similar viscoelastic recoil in the local fluid velocity is observed in both experiments and simulations of the start-up of steady shear flow [19]. Both models exhibit a range of times over which the kink velocity is out of phase with the wall forcing, but the range is more confined, and the effect is sharper and more pronounced in the VCM model than in the PEC model. This out of phase response represents the elastic recoil of the system. At the higher frequency ($De = 2\pi$) these differences become further highlighted. In both models the wall velocity and the kink velocity are out of phase with each other for large portions of each cycle; however the amplitude of the recoil and overshoot events

(at $t \approx 0.4$) are larger and more rapidly damped in the VCM model. Flow reversal at the kink occurs for the VCM model at $Det = 0, \pi$ for $De = 2\pi$; this is evidenced in Fig. 2D as well as in Fig. 4. In contrast at these particular times the kink motion for the PEC model is still in phase with the wall forcing.

In Fig. 5 we increase the driving frequency still further, to $De = 10\pi$, and concomitantly the shear rates have also been increased to $Wi = 40, 60$ in order to stay within the shear banding regime. The VCM and PEC models behave quite differently at this frequency. The response of both models is slow compared to the forcing time scale, so there is insufficient time for the material to recover and approach a quasi-steady state response at any point during the cycle. The larger viscous contribution to the stress in the PEC model results in a velocity profile which becomes increasingly diffusive in character and the location of any kink becomes difficult to discern (at $Wi = 40$ the kink in the PEC model is very close to the left boundary, that is shear banding is just initiating at this Wi). The banding of the VCM model is still distinct and sharp due to the additional localization associated with rupture of the 'A' chains and the lower background solvent viscosity.

The effective relaxation time for the VCM model in LAOS is $\lambda_{eff}/\lambda_A = 1/(1+ c_{Aeq} + \frac{2\xi Wi A_{r\theta}}{3n_A})$, whereas for the PEC model, $\lambda_{eff}/\lambda_A = 1/(1 + \frac{2\xi Wi A_{r\theta}}{3})$ (here $A_{r\theta}$ is the appropriate time and space evolved shear stress for the respective model). Due to the appearance of a nonzero c_{Aeq} in the denominator and the additional contribution from the decrease in the number density of 'A' chains in strong deformation, this dynamic effective relaxation time for the VCM model is smaller than for the PEC model in the high shear rate region. For low frequencies both dynamic relaxation times are smaller than the time scale of the imposed motion $\lambda_{eff}/\lambda_A << \frac{1}{De}$, but as the frequency increases

the balance shifts to $(\lambda_{eff}/\lambda_A)_{VCM} < \frac{1}{De} < (\lambda_{eff}/\lambda_A)_{PEC}$. This explains the difference in response of the two models at $De = 0.2\pi$ and 2π as seen in Fig. 3, 4. At the lower frequency the two velocity profiles are very similar and the flow is effectively quasi-steady except at the localized recoil events. In both cases the time scale of the imposed motion is long compared to the dynamic breakage time. However for the higher frequency as the shear rate is increased it is evident that the PEC model has not had time to fully relax to a quasi-steady profile at any point during the cycle.

The shear stress profiles for the (long) 'A' species for the VCM model, and the entangled polymer contribution to the stress for the PEC model are shown in Fig. 6, along with the corresponding local number density of the (long) 'A' species for the VCM model at $De = 2\pi, Wi = 20$. The snapshots are shown at the same times as the velocity profiles in Fig. 3. As anticipated, in the high shear rate band (near the inner wall) the 'A' chains have broken, the local number density n_A is small and the resultant shear stress from the A species is small. The shear stress for the PEC model varies qualitatively in the same way as observed for the VCM model (with small differences in the phase at intermediate times) for this selection of frequency and imposed shear rate; however, the magnitude of the stress in high shear rate band for the PEC model is larger than the contribution to the stress from the long 'A' species for the VCM model as anticipated due to the breakage in the VCM model.

It is clear from Figs. 2-5 that the dynamics of the shear-banding transition in LAOS are a function of both the time-scale of deformation and the imposed deformation rate (or strain amplitude). These interdependencies can be better understood physically if the computational results are assembled into a *Pipkin diagram* [21, 26], as shown in Fig. 7(a) and 7(b). For each value of De we plot

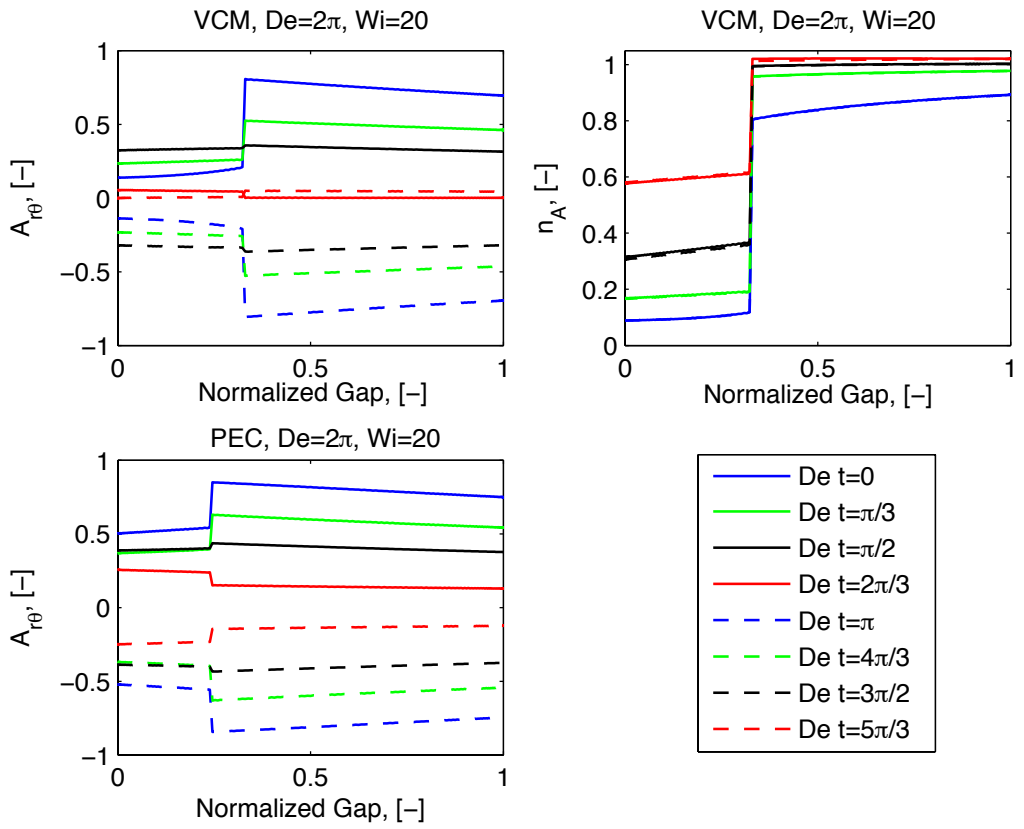

Fig. 6. Profiles of the shear stress contribution from the entangled long chains for the VCM model (upper left) and the PEC model (lower row). The profiles are plotted at the same points within the cycle as shown in Figs. 3, 5, and the same frequency and shear rate as shown in Fig. 4 right. On the upper right is the corresponding instantaneous number density profile of the VCM long chains at the same times and parameter values.

the critical dimensionless strain rate Wi_{c1} for onset of shear banding and a second critical strain rate Wi_{c2} at which a banded velocity profile can no longer be discerned because the high rate band fills the entire gap. Results are shown for both the VCM and the PEC model. The (De, Wi) coordinates of the individual velocity profiles of the VCM model shown in Fig. 2 are indicated in Fig. 7(a) by the labeled points. Within the region delineated by the dashed

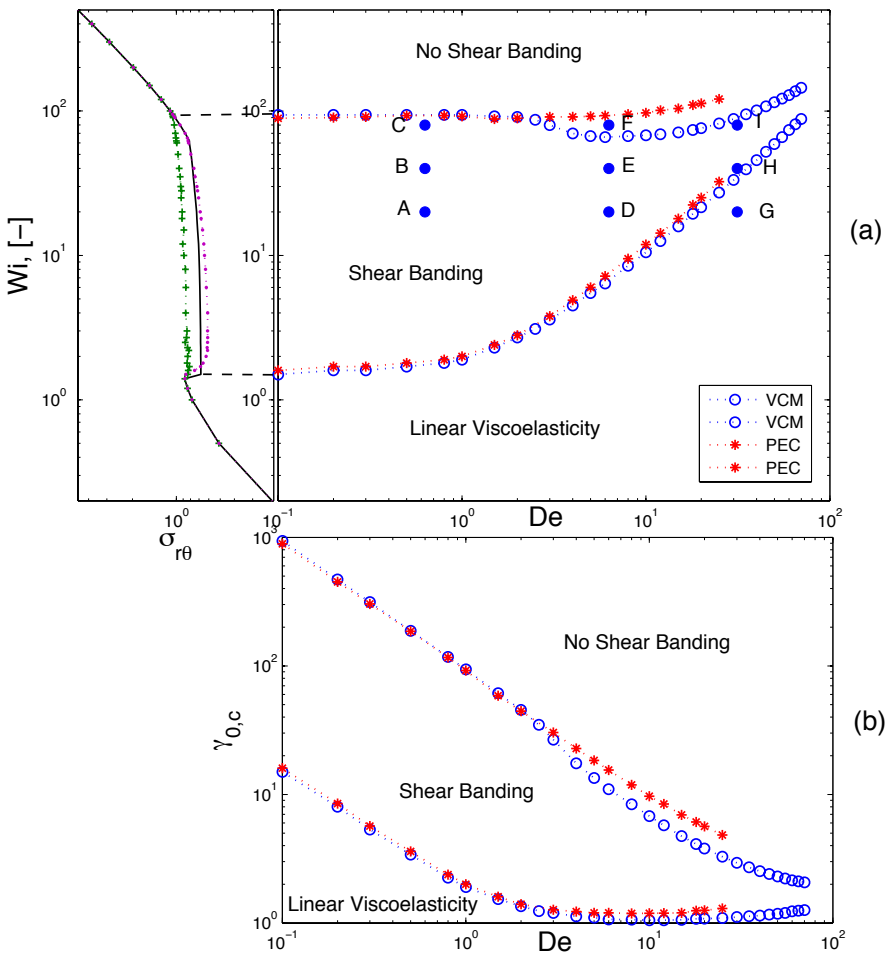

Fig. 7. Pipkin diagram showing the LAOS response of entangled fluids described by the VCM model, and a comparison with the predictions of the PEC model (with parameters as given in Fig. 1). Labeled points A-I as in Fig. 2. Open circles in (a) bound the shear banding region in strain rate/ frequency (De, Wi) space for the VCM model, starred symbols bound the region for the PEC model. The open circles in (b) enclose the same region in strain/frequency (De, γ_0) space for the VCM model, starred symbols for the PEC model. At the left of (a) we show the steady state profile of the shear stress for the VCM model. The solid line corresponds to the solution with small diffusion ($\delta = 0.001$), the other two curves correspond to the result with no diffusion with a ramp start up ($v|_{wall} = v_w \tanh at$) which is slow ($a = 0.1$; green, + symbols) and fast ($a = 10$; purple closed symbols).

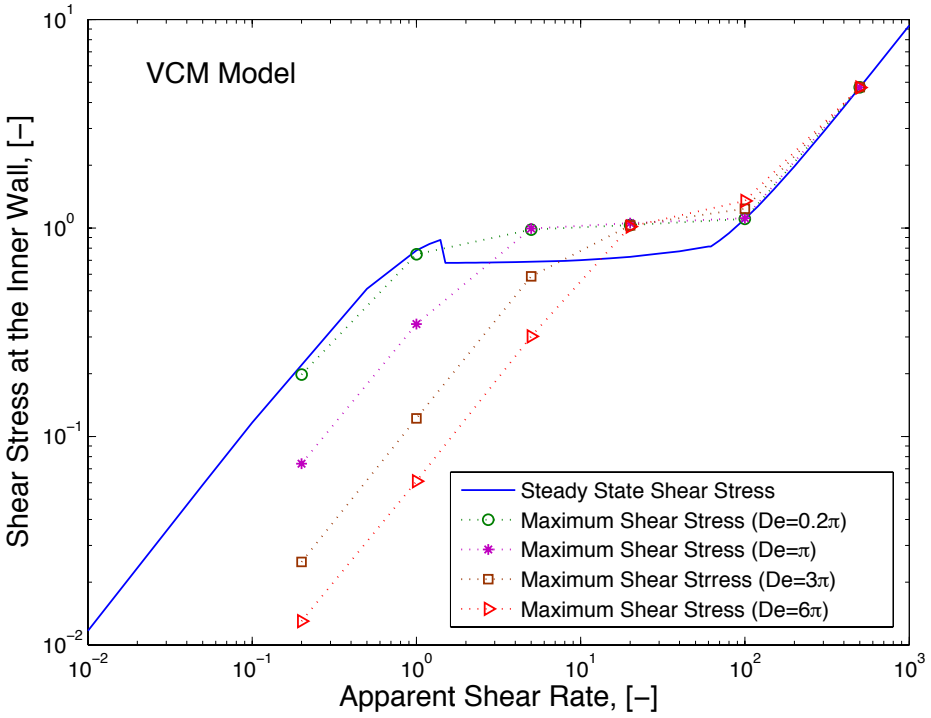

Fig. 8. Maximum wall shear stress as a function of imposed shear rate predicted by the VCM model for frequencies as indicate. The blue line is the steady state response for the parameters shown in Fig. 1.

lines, the velocity field in the entangled fluid exhibits inhomogeneities with varying degrees of shear banding; below and above this region there is no shear banding. The precise spatial location of the shear band can be observed visually in most cases, or it can be monitored numerically by seeking the extremum of $\frac{\partial \dot{\gamma}}{\partial r}$. Computations at A, B of Fig. 2, for example, show $\frac{\partial \dot{\gamma}}{\partial r} \sim 10^4$, representing the extent to which the numerical method can resolve the discontinuous change in $\dot{\gamma}(r)$ at the location of the shear band.

For small Weissenberg numbers ($Wi < 1.5$) there is no shear banding for any value of De, the fluid response to the oscillatory forcing at the wall is a purely homogeneous shear flow. At very high oscillatory frequencies within the

inhomogeneous region the 'banding' event for the PEC model has insufficient time in each cycle to develop. It is thus increasingly difficult in this regime to accurately discern the boundaries demarcating the presence or absence of shear-banding. The VCM model, on the other hand, has a sharp banding response even in these regions.

At the higher oscillatory frequencies, the rapid temporal variations in the wall velocity shifts the lower boundary for onset of shear-banding to higher critical Weissenberg numbers. This behavior can be more clearly understood with reference to Fig. 7(b) in which the critical strain amplitudes for banding, $\gamma_{0,c} = Wi_c/De$, are shown as a function of De. At low frequencies, the deformation is slow compared to the relaxation time of the entangled microstructure ($1/\omega \gg \lambda_A$) and fluid elements continually relax during each period of oscillatory straining. Thus very large strains can be accumulated in the entangled material before shear-banding occurs. By contrast, at larger Deborah numbers, molecular relaxation is insignificant and the response is dominated by the nonlinear elastic response: banding occurs when a constant critical strain $\gamma_{0,c1} \approx 1.1$ is exceeded. The smooth transition between these two asymptotic regimes can be described quite accurately (for $0 < De \leq 20$) by the expression $Wi_{c1} = 1.1De + 1.5e^{-De/2}$. At very high frequencies ($De > 20$) the bottom boundary slowly curves up due to the additional stabilizing contributions of viscous stresses.

The upper boundary for the shear-banding transition remains relatively flat at $Wi_{c2} \approx 90$ for the PEC model. Above this critical value of the Weissenberg number, the additional stress carried by the purely viscous 'B' species exceeds the contribution from the longer 'A' species, which is increasingly disentangled by the high shear rate in the fluid. A detailed consideration of the momentum

Eqn. (9) in this limit shows that the velocity field can vary smoothly across the gap and still satisfy the required radial variation in the total shear stress $\sigma_{r\theta}(r)$ across the gap. For the VCM model we see that at a frequency of about $De = 1.5$ the upper boundary of the shear banding region first decreases slightly, then at $De = 10$ it begins to rise; eventually rising above that of the PEC model. This frequency dependence in the upper boundary at high De is expected due to the additional stress contributions of the (viscoelastic) 'B' species. This can be understood more clearly in figure 7(b) where the upper boundary of the shear banding region for the VCM model in the strain versus frequency diagram is seen to decrease faster than that of the PEC model, before leveling off.

An alternative representation of these results is shown in Fig. 8 where the LAOS analogue of the steady shear "flow curve" of Fig. 1 is shown for the VCM model. For each apparent shear rate (Wi) across the gap, the maximum value of the shear stress at the wall within a cycle is plotted. Note that as the frequency is increased the plateau region shrinks from the low shear rate boundary, and the plateau level for these selected values rises to the height of the overshoot observed in the steady state shear-stress plateau. Well before they approach this plateau, these curves are each linear and parallel on this log-log plot. In this linear viscoelastic regime ($Wi \lesssim 1$) the stress growth in a transient shear flow is of the form $\sigma' \approx G\gamma(t)$. Furthermore, in a periodic flow such as oscillatory shear flow, the maximum strain is reached at a time $t'_{max} \approx \frac{\pi}{2\omega}$ and the strain accumulated in this time is $\gamma_{max} \approx \gamma_0 \omega t'_{max}$. Combining these approximate expressions gives, to the lowest order, $\sigma'_{max} \approx G\gamma_0\omega\frac{\pi}{2\omega}$, or in dimensionless form $\sigma_{max} \approx \frac{\pi}{2}\frac{Wi}{De}$.

The graph on the left of Fig. 7(a) shows the steady state flow curve prediction

of dimensionless shear stress $\sigma_{r\theta}$ predicted by the VCM model as a function of dimensionless shear rate $Wi = \lambda_A \dot{\gamma}$. Note that for the VCM model, as reported in [19] for the PEC model, the shape of the flow curve in the absence of diffusion depends on the initial conditions. Similar trends are observed in other nonlocal models [12, 13]. Three curves are shown: the solid line is the VCM model prediction with a small ($\delta = 0.001$) diffusion, the plus symbols are the result with no diffusion but with a slow initial ramp up to the final wall velocity ($\tanh(0.1t)$), and the solid symbols are the result with no diffusion but a faster ramp up to the final wall velocity ($\tanh(10t)$). In the case of slow start-up, the steady state plateau stress is larger than the value obtained with a fast start up ramp, and higher than the unique plateau obtained with diffusion. In the case of slow start-up the plateau also ends at a higher shear rate than for the faster start up. Similar trends hold in the PEC model, but are far less pronounced and are not shown here. These observations are relevant to the upper boundary of the Pipkin diagram shown in Fig. 7(a). For the PEC model the upper boundary of the shear-banding transition in Fig. 7(a) remains relatively flat at $Wi_{c2} \approx 90$. For the VCM model the upper boundary is flat for small frequencies with a critical value which is consistent with the steady state flow curve obtained using a *slow* ramped start-up. This boundary then decreases to a lower value at $De \approx 6$ corresponding to a shear rate value consistent with the termination of the steady flow plateau for the *faster* ramp. After this local dip the curve then rises again for $De \gtrsim 10$ due to viscous stresses. This behavior is mirrored in the critical strain/frequency diagram shown in Fig. 7(b): the upper boundary of the shear banding region for the VCM model appears to asymptote to a critical strain of $\gamma_{0,c} \approx 2$ at high frequencies. At these shear rates the PEC model behavior has become too diffusive for one to readily observe banding behavior.

4 Phase Plane (Lissajous) Curves

In addition to probing the kinematics of shear banding in LAOS, our model computations also provide insight into the evolution of the shear stress $\sigma(t; De, Wi)$ acting on the oscillating wall of the Couette device. The total oscillatory shear stress can be conveniently portrayed by a phase plane representation in the form of a Lissajous figure with stress being plotted against the instantaneous strain $\gamma(t)$ as shown in Fig.9 or, equivalently, against the strain rate $\dot{\gamma}(t)$ as shown in Fig.10. At small strain amplitudes, below the critical boundary $\gamma_{0,c1}$ shown in Fig. 7(b), the VCM model predicts a linear viscoelastic response at all frequencies and the Lissajous trajectories are simple ellipses. A representative example is shown at $De = 10\pi, Wi = 20$. The purely elastic contribution to the total viscoelastic stress is shown in Fig. 9 by the red (dashed) lines [27]. The VCM model predicts a linear elastic contribution at small γ_0 but this becomes increasingly nonlinear at larger imposed strains. Beyond the critical strain corresponding to the onset of shear banding ($Wi > 1.7$ at $De = 0.2\pi$ or $Wi > 6.5$ at $De = 2\pi$) the trajectories become increasingly nonlinear with local overshoots in the instantaneous shear stress. As the oscillatory frequency increases, the system response becomes progressively more in phase with the applied strain and the magnitude of the viscous response (corresponding to the difference between the total stress (solid line) and the elastic stress (broken line)) decreases. At intermediate Deborah numbers $De \approx 2\pi$ intracycle strain softening, then hardening is observed. In the Lissajous curves, when plotted in a viscous representation (i.e. against shear rate $\dot{\gamma}(t)$), secondary loops appear. These secondary loops further represent the strong elastic nonlinearity as discussed in [28]. Harmonic analysis of the stress signal in this

regime shows a rapid growth in the magnitude of the third and fifth Chebyshev coefficients (which becomes a factor of two larger than the first order coefficient) further indicating the strong nonlinear elastic response (see Appendix Fig. 1). This behavior is in direct contrast to that for the non-shear banding Giesekus model [28], in which the fifth order elastic coefficient stays smaller than the third order which stays smaller than the first order coefficients. A detailed comparison of the magnitude of the coefficients in the PEC model shows that, like the Giesekus model, the fifth order harmonic contributions remain smaller than the third order, which are themselves smaller than the leading order coefficients.

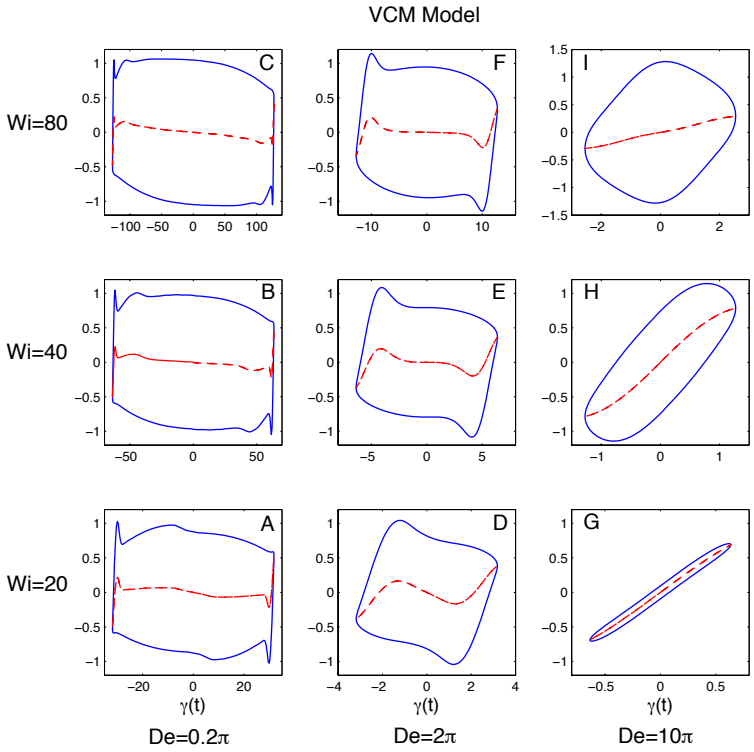

Fig. 9. Lissajous figures of the oscillatory stress responses for the VCM model as a function of the (apparent or nominal) imposed strain $\gamma(t) = \gamma_0 \sin De\, t$. The plots are at the same frequencies and strains as those shown in Fig. 2, and are identified by the corresponding letters in the Pipkin diagram (Fig. 7).

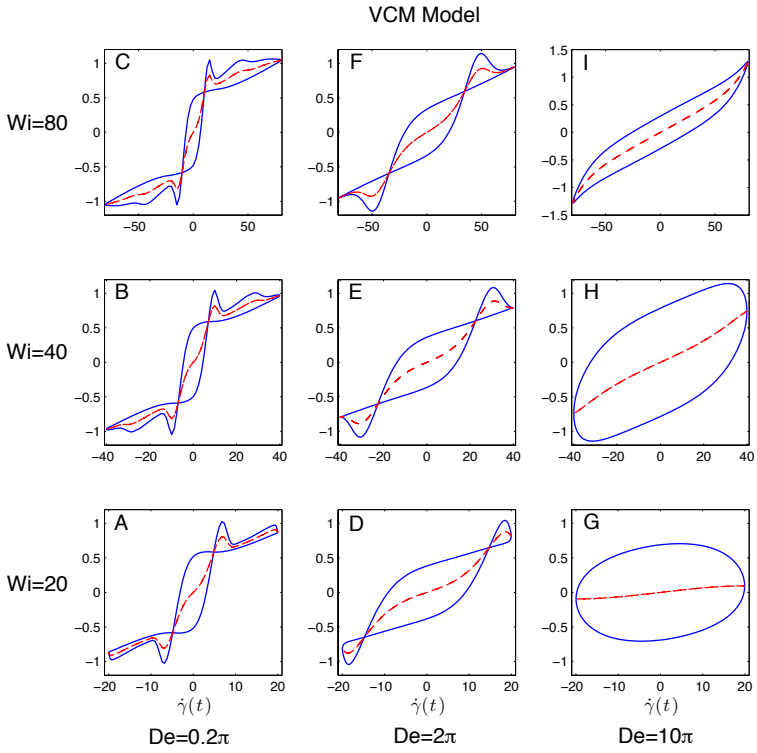

Fig. 10. Lissajous figures of the oscillatory stress responses of the VCM model as a function of the (apparent or nominal) imposed strain rate $\dot{\gamma}(t) = \gamma_0 De \sin De\, t$. The plots are at the same frequencies and strains as those shown in Fig. 2, and are identified by the corresponding letters in the Pipkin diagram (Fig. 7).

5 Conclusion

In this paper we have demonstrated how a relatively-simple class of rheological equations of state—derived from a self-consistent kinetic network theory treatment of microstructural deformation and its coupling to the total state of stress in the system [16, 19]—can describe the dynamics of shear-banding transitions in a broad class of time-varying shearing flows. Large amplitude oscillatory shear (LAOS) provides a means to independently control both the amplitude and time scale of the imposed deformation, and the resulting 'state space' of the shear-banded structures can be conveniently represented in terms

of a Pipkin diagram. The key features of the shear-banding predicted in LAOS by the PEC model are in good qualitative agreement with experimental measurements using monodisperse entangled polymer solutions [7]. The LAOS test protocol also provides a way to distinguish between different limiting cases of the VCM family of models (VCM vs PEC) and should be of interest in experimental probes of the nonlinear rheology of entangled systems; as well as enabling a more discriminating test of the predictions of putative rheological equations of state for nonlinear viscoelastic fluids[29]. The increased nonlinearity of the two species VCM model over that of the PEC model leads to spatially well-defined versus diffusive banding profiles at higher frequencies; as well as changes in the upper boundary of the Pipkin diagram.

6 Acknowledgements

The authors acknowledge the support of the National Science Foundation under NSF DMS-0807395 and 0807330 and Dr. R.H. Ewoldt for helpful discussions.

A Chebyshev Coefficients

In the Chebyshev decomposition ($\sigma'(t;\omega,\gamma_0) = \gamma_0\Sigma_k(e_k(\omega,\gamma_0)T_k(sin(\omega t)) + \omega\nu_k(\omega,\gamma_0)T_k(cos(\omega t))))$ of the LAOS responses any coefficients that are higher than the first order indicate the nonlinearity in the system. Fig. A.1(a), (b) shows the computed ratio of the third and fifth order elastic and viscous coefficients, respectively, to the first order coefficients for one frequency choice, $De = 2\pi$. The first order elastic and viscous coefficients are plotted in Fig.

A.1(c). Also shown by the broken line is the critical strain $\gamma_{0,c}$ corresponding to onset of shear-banding at this Deborah number. It is clear from the ratio ν_3/ν_1 that a viscous intra-cycle nonlinear shear-thickening rheological response (albeit small) can be observed before the onset of shear banding. A magnitude smaller ($O(10^{-2})$, not visible in the scale of the figure) elastic softening occurs at the same strain. Following the onset of shear-banding, the nonlinearity of the Lissajous phase portraits increases dramatically with very large values of e_3/e_1 and e_5/e_1 that arise from the phase-shifted oscillations of the shear-bands shown in Fig. 3, 5.

References

[1] S. M. Fielding. Complex dynamics of shear banded flows. *Soft Matter*, 2:1262–1279, 2007.

[2] P. D. Olmsted. Perspectives on shear banding in complex fluids. *Rheol. Acta*, 47:283–300, 2008.

[3] M. M. Britton and P. T. Callaghan. Two-phase shear band structures at uniform stress. *Phys. Rev. Lett.*, 78:4930–4933, 1997.

[4] M. M. Britton, R. W. Mair, R. K. Lambert, and P. T. Callaghan. Transition to shear banding in pipe and Couette flow of wormlike micellar solutions. *J. Rheol.*, 43:897–909, 1999.

[5] J. B. Salmon, A. Colin, S. Manneville, and F. Molino. Velocity profiles in shear-banding wormlike micelles. *Phys. Rev. Lett.*, 90:228303–1 – 228303–4, 2003.

[6] P. Tapadia and S-Q. Wang. Direct visualization of continuous simple shear in non-Newtonian polymeric fluids. *Phys. Rev. Lett.*, 96:016001–1 – 016001–4, 2006.

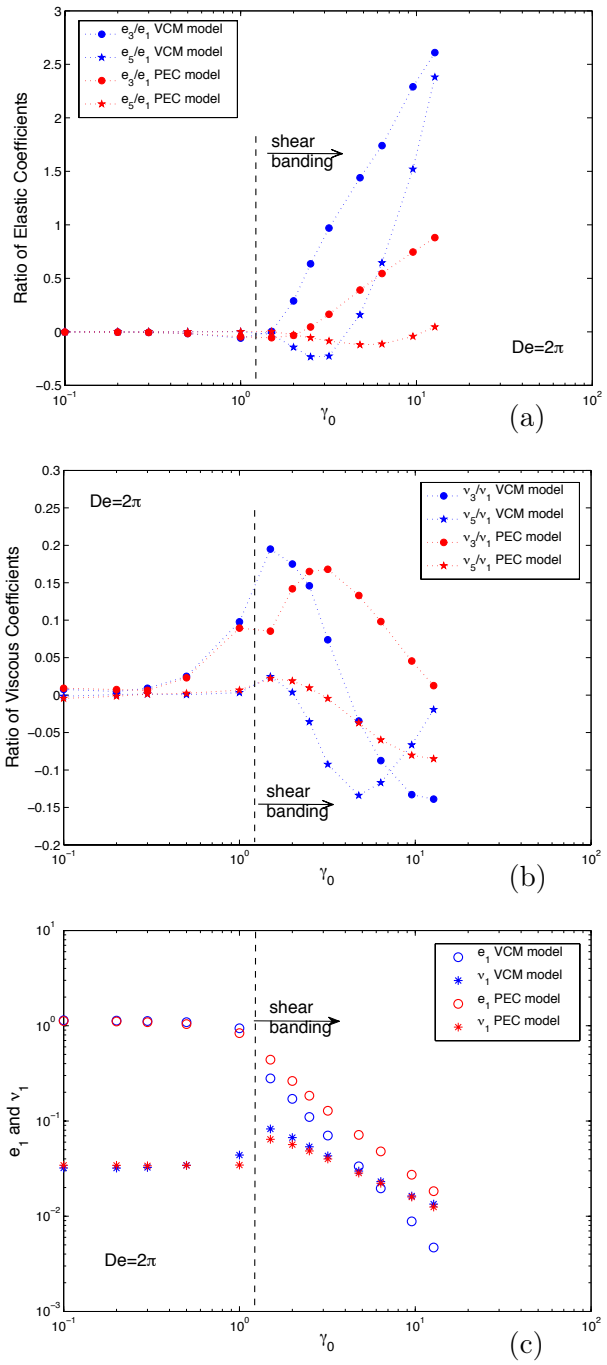

Fig. A.1. (a). The ratio of the third order and fifth order elastic coefficients to the first order elastic coefficients for the VCM and PEC model. (b). The ratio of the third order and fifth order viscous coefficients to the first order viscous coefficients for the VCM and PEC model. (c). The first order elastic and viscous coefficients for the VCM and PEC model. The model parameters are given in Fig. 1, $De = 2\pi$.

[7] P. Tapadia, S. Ravindranath, and S-Q. Wang. Banding in entangled polymer fluids under oscillatory shearing. *Phys. Rev. Lett.*, 96:196001–1–196001–4, 2006.

[8] E. Miller and J. P. Rothstein. Transient evolution of shear banding in wormlike micelle solutions. *J. Non-Newtonian Fluid Mech.*, 143:22–37, 2007.

[9] R. Ganapathy and A. K. Sood. Intermittency route to rheochaos in wormlike micelles with flow-concentration coupling. *Phys. Rev. Lett.*, 96:108301, 2006.

[10] S. M. Fielding and P. D. Olmsted. Nonlinear dynamics of an interface between shear bands. *Phys. Rev. Lett.*, 96:104502, 2006.

[11] J. F. Berret, D. C. Roux, and G. Porte. Isotropic-to-nematic transition in wormlike micelles under shear. *J. Phys. II France*, 4:1261–1279, 1994.

[12] C.-Y. David Lu, Peter D. Olmsted, and R. C. Ball. Effects of nonlocal stress on the determination of shear banding flow. *Phys. Rev. Lett.*, 84:642–645, 2000.

[13] P.D. Olmsted, O. Radulescu, and C.Y.D. Lu. Johnson-Segalman model with a diffusion term in cylindrical Couette flow. *J. Rheol.*, 44:257–275, 2000.

[14] J. K. G.Dhont and W. J. Briels. Gradient and vorticity banding. *Rheol. Acta*, 47:257–281, 2008.

[15] N. A. Spenley, M. E. Cates, and T. C. B. McLeish. Nonlinear rheology of wormlike micelles. *Phys. Rev. Lett.*, 71:939–942, 1993.

[16] P. A. Vasquez, L. P. Cook, and G. H. McKinley. A network scission model for wormlike micellar solutions I: Model formulation and homogeneous flow predictions. *J. Non-Newtonian Fluid Mech.*, 144:122–139, 2007.

[17] J.M. Adams and P.D. Olmsted. Nonmonotonic models are not necessary

to obtain shear banding phenomena in entangled polymer solutions. *Phys. Rev. Lett.*, 102:067801, 2009.

[18] R. G. Larson. *Constitutive Equations for Polymer Melts and Solutions*. Butterworths Series in Chemical Engineering, ed. H. Brenner. Butterworths, Boston, 1988.

[19] L. Zhou, P. A. Vasquez, L. P. Cook, and G. H. McKinley. Modeling the inhomogeneous response and formation of shear bands in steady and transient flows of entangled liquids. *J. Rheol.*, 52:591–623, 2008.

[20] M. Cromer, L.P. Cook, and G.H. McKinley. Extensional flow of wormlike micelles. *Chemical Engineering Science*, 64:4588–4596, 2009.

[21] J.M. Dealy and K.F. Wissbrun. *Melt Rheology and its Role in Plastics Processing: Theory and Applications*. Van Nostrand Reinhold, New York, 1990.

[22] H.G. Sim, K.H. Ahn, and S.J. Lee. Large amplitude oscillatory shear behavior of complex fluids investigated by a network model: A guideline for classification. *J. Non-Newtonian Fluid Mech.*, 112:237–250, 2003.

[23] R. Ewoldt, A.E. Hosoi, and G.H. McKinley. Rheological fingerprinting of complex fluids using large amplitude oscillatory shear (LAOS) flow. *Annual Transactions of the Nordic Rheology Society*, 15:3–8, 2007.

[24] R. G. Larson. A constitutive equation for polymer melts based on partially extending strand convection. *J. Rheol.*, 28:545–571, 1984.

[25] P. E. Boukany and S-Q. Wang. Use of particle-tracking velocimetry and flow birefringence to study nonlinear flow behavior of entangled wormlike micellar solution: From wall slip, bulk disentanglement to chain scission. *Macromolecules*, 41:1455–1464, 2008.

[26] M. Parthasarathy and D. J. Klingenberg. Large amplitude oscillatory shear of er suspensions. *J. Non-Newtonian Fluid Mech.*, 81:83–104, 1999.

[27] R. H. Ewoldt, A. E. Hosoi, and G. H. McKinley. New measures for characterizing nonlinear viscoelasticity in large amplitude oscillatory shear. *J. Rheol.*, 52:1427–1458, 2008.

[28] R. H. Ewoldt and G. H. McKinley. On secondary loops in laos via self-intersection of lissajous-bowditch curves. *Rheol. Acta*, 49:213–219, 2010.

[29] R. S. Jeyaseelan and A. J. Giacomin. Network theory for polymer solutions in large amplitude oscillatory shear. *J. Non-Newtonian Fluid Mech.*, 148:24–32, 2008.